Annals of Glaciology



Paper

Cite this article: Jordan TM, Schroeder DM, Elsworth CW, Siegfried MR (2020). Estimation of ice fabric within Whillans Ice Stream using polarimetric phase-sensitive radar sounding. Annals of Glaciology 1–10. https://doi.org/10.1017/aog.2020.6

Received: 2 August 2019 Revised: 6 January 2020 Accepted: 7 January 2020

Kevwords

Anisotropic ice; radio-echo sounding; ice crystal studies; ice streams

Author for correspondence:

Thomas M. Jordan, E-mail: tom.jordan@bris. ac.uk

© The Author(s) 2020. This is an Open Access article, distributed under the terms of the Creative Commons Attribution licence (http://creativecommons.org/licenses/by/4.0/), which permits unrestricted re-use, distribution, and reproduction in any medium, provided the original work is properly cited.

Estimation of ice fabric within Whillans Ice Stream using polarimetric phase-sensitive radar sounding

Thomas M. Jordan^{1,2}, Dustin M. Schroeder^{1,3}, Cooper W. Elsworth¹ and Matthew R. Siegfried^{1,4}

¹Department of Geophysics, Stanford University, USA; ²School of Geographical Sciences, University of Bristol, UK; ³Department of Electrical Engineering, Stanford University, USA and ⁴Department of Geophysics, Colorado School of Mines, USA

Abstract

Here we use polarimetric measurements from an Autonomous phase-sensitive Radio-Echo Sounder (ApRES) to investigate ice fabric within Whillans Ice Stream, West Antarctica. The survey traverse is bounded at one end by the suture zone with the Mercer Ice Stream and at the other end by a basal 'sticky spot'. Our data analysis employs a phase-based polarimetric coherence method to estimate horizontal ice fabric properties: the fabric orientation and the magnitude of the horizontal fabric asymmetry. We infer an azimuthal rotation in the prevailing horizontal c-axis between the near-surface ($z \approx 10$ –50 m) and deeper ice ($z \approx 170$ –360 m), with the near-surface orientated closer to perpendicular to flow and deeper ice closer to parallel. In the near-surface, the fabric asymmetry increases toward the center of Whillans Ice Stream which is consistent with the surface compression direction. By contrast, the fabric orientation in deeper ice is not aligned with the surface compression direction but is consistent with englacial ice reacting to longitudinal compression associated with basal resistance from the nearby sticky spot.

1. Introduction

There are two components to ice-sheet motion: internal deformation (governed by ice rheology) and basal sliding (governed by basal properties and subglacial hydrology). The rheology of ice is dependent upon ice temperature and ice fabric (the orientation distribution of ice crystals) (Azuma, 1994). The ice fabric provides a record of past deformation and significantly influences the viscosity of ice during future deformation (Alley, 1988). Our understanding of ice fabric within the polar ice sheets is primarily informed by measurements from ice cores underneath ice divides and domes, which have low ice velocities (Wang and others, 2002; Fujita and others, 2006; Montagnat and others, 2014). This geographic limitation on direct observations of ice fabric limits our understanding of how fabric impacts ice dynamics and suggests a need for new geophysical methods for investigating ice fabric and its dependence and influence on ice flow across different flow regimes.

Ice fabric anisotropy results in dielectric anisotropy (birefringence), which can be detected using polarimetric radar sounding (Hargreaves, 1977). However, similar to ice core fabric measurements, radar sounding studies of ice fabric have focused on slow-flowing regions of the ice sheets (Fujita and others, 2006; Drews and others, 2012; Matsuoka and others, 2012; Li and others, 2018). In recent years the Autonomous phase-sensitive Radio-Echo Sounder (ApRES) has become widely used by glacier geophysicists when they perform ground surveys. The ApRES was originally designed to estimate basal melt and vertical strain rates (Nicholls and others, 2015) and has since been used to investigate englacial water storage (Kendrick and others, 2018), englacial layer geometry (Young and others, 2018), and to invert for ice flow velocities (Kingslake and others, 2016). The ApRES has recently been used to conduct polarimetric radar sounding measurements in complex flow regions, with Brisbourne and others (2019) focusing on ice rises in the Weddell sea sector of Antarctica.

As a phase-coherent radar system, polarimetric measurements from an ApRES can be used to determine ice fabric properties using a polarimetric coherence framework (Dall, 2010; Jordan and others, 2019). This phase-based method has previously been applied to airborne measurements from the POLarimetric Airborne Radar Ice Sounder (POLARIS) (Dall and others, 2009; Vazquez-Roy and others, 2012), and a ground-based version of the Multi Channel Coherent Radar Depth Sounder (MCRDs) (Li and others, 2018). The method enables estimation of ice fabric properties in the horizontal plane, formulated in terms of a second-order orientation tensor which describes the crystallographic/c-axis orientation distribution (Woodcock, 1977; Montagnat and others, 2014). Using radar phase to directly estimate ice fabric represents a departure from past power-based analyses (Hargreaves, 1977; Fujita and others, 2006; Matsuoka and others, 2012; Li and others, 2018), which can suffer from angular ambiguity when inferring the prevailing fabric orientation (Fujita and others, 2006; Matsuoka and others, 2012).

The goal of this study is to assess the potential of using the ApRES and the polarimetric coherence method to estimate ice fabric within ice streams. Fabric in ice streams has previously

been characterized through direct sampling (Jackson and Kamb, 1997) or seismic measurements (Horgan and others, 2011; Diez and Eisen, 2015; Picotti and others, 2015; Smith and others, 2017). These studies indicate that a range of different fabric types can form in ice streams and there is a general lack of consensus regarding what is 'typical' ice-stream fabric. In addition, ice-stream flow mechanics studies have inferred marked spatial variation in ice fabric along flow (Minchew and others, 2018) and have highlighted the role of ice fabric in modifying marginal shear-stress (Jackson and Kamb, 1997). Further quantifying the effects of ice fabric on fast ice flow is also an important precursor to introducing more complete physics into large-scale ice-sheet simulations (Hay, 2017).

As a case study of the polarimetric coherence method applied to fast ice flow, we focus upon a ground-based traverse across Whillans Ice Stream, West Antarctica. The analyses enable us to estimate ice fabric in selected regions of the ice column and compare estimates in the near-surface ($z \approx 10$ –50 m) to deeper ice ($z \approx 150$ –400 m). The results indicate that ice fabric can develop across relatively small spatial scales in fast ice flow (both between measurement sites and within the ice column).

2. Experimental Method

2.1. Radar system

The ApRES is a FMCW (Frequency-Modulated Continuous-Wave) radar with bandwidth, B = 200 MHz and center frequency, $f_c = 300$ MHz. The classical range resolution of ApRES is

$$R = \frac{c}{2B\sqrt{\epsilon_{\rm ice}}},\tag{1}$$

 ≈ 0.43 , where $\epsilon_{\rm ice} \approx 3.15-3.18$ is the (real, polarization-averaged) dielectric permittivity of ice and c is the vacuum radio-wave speed. The instrument also has the capacity to measure sub-range-resolution precision using a Vernier technique but we do not do so here. The instrument stores the de-ramped signal which has phase

$$\phi_{\rm d} = \phi_{\rm t} - \phi_{\rm r},\tag{2}$$

where ϕ_t is the transmitted phase and ϕ_r is the received phase. The impact of signal de-ramping upon the coherence method is discussed later. An in-depth technical summary of the ApRES is provided by Brennan and others (2014).

2.2. Radar survey and measurements

Our study is located on the downstream reaches of Whillans Ice Stream, on the Siple Coast of West Antarctica (Fig. 1) and bounded to the grid northeast by the suture zone with the neighboring Mercer Ice Stream. These two ice streams originate from separate catchments, and merge over Whillans Ice Plain. The streamlines, derived from velocity measurements (Rignot and others, 2011, 2017), illustrate the suture zone between ice streams that begins with the coalescence of Whillans and Mercer shear margins. The approximate location of a basal sticky spot (Luthra and others, 2016) is also marked. The ground-based ApRES survey consists of a traverse of ten sites collected on 12 December 2016 that cross the suture zone dividing the two ice stream trunks. The site numbering is from grid east to grid west increasing upstream toward the sticky spot. The ice thickness across the traverse ranges from $z \approx 715$ m (Site 10) to $z \approx 810$ m (Site 1).

At each site, co-polarized measurements (conducted with the transmit and receive antennas in the same orientation) were

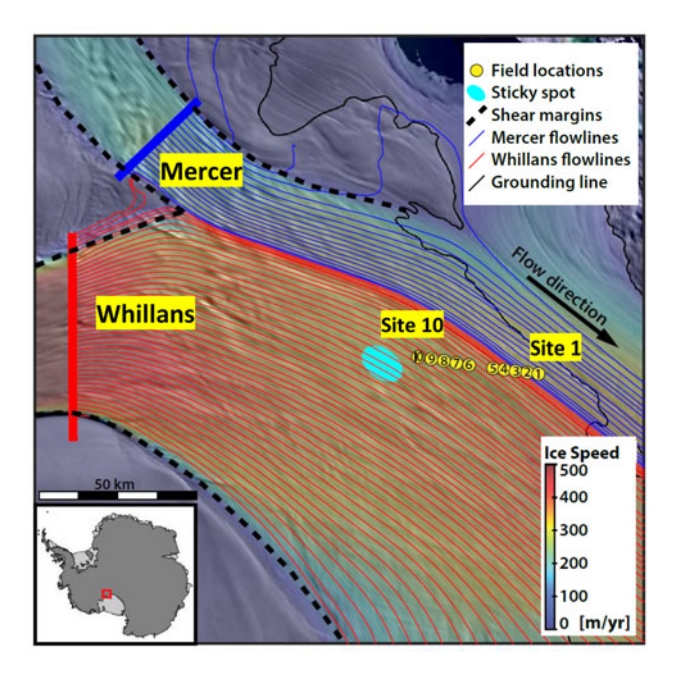
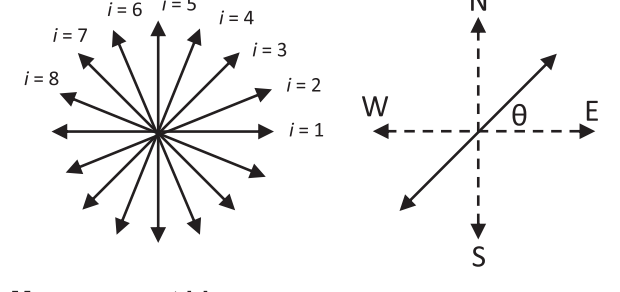


Fig. 1. Field setting of Whillans and Mercer ice streams on the Siple Coast, West Antarctica. The radar ground survey measurement sites are shown as numbered yellow dots. Streamlines from Whillans (red) and Mercer (blue) ice streams are derived from ice velocity (Rignot and others, 2011, 2017). Background image shows ice velocity over a mosaic of MODIS visible satellite imagery (Haran and others, 2005).



Measurement bins Definition of bearing angle

Fig. 2. (a) Multi-polarization plane measurements. (b) Definition of bearing angle.

made using an established multi-polarization plane set-up (Fujita and others, 2006; Matsuoka and others, 2012). This procedure consisted of measurements at a 22.5° angular resolution over the interval [0, 157.5]° with the azimuthal bearing angle, θ , defined as the angle between the polarization plane and due east in a counter-clockwise direction (Fig. 2). There are therefore eight independent polarization planes at $\theta = 0$, 22.5, 45...157.5° which are indexed using i = 1, 2, 3...8. The horizontal baseline separation between receive and transmit antennas was approximately 10 m. During data collection θ was measured with respect to magnetic north/west, and was later corrected for magnetic declination (ranging from $\approx 100-120^\circ$ east) to recover true north/west.

2.3. Polarimetric data analysis

In this study we compare analyses of the polarimetric coherence alongside the polarimetric power and we now outline how these variables are computed from the ApRES data. A more detailed description of how these variables are related to ice fabric anisotropy is described in the Theoretical Background section.

2.3.1. Polarimetric coherence

When there is horizontal anisotropy in the ice fabric, polar ice behaves as a birefringent material for a vertically propagating

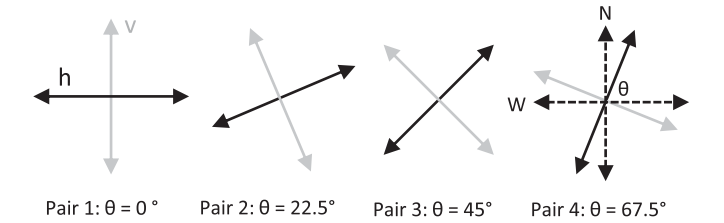


Fig. 3. Definition of h-v pairs in polarimetric coherence calculations.

radio wave. In this scenario, referred to as 'birefringent propagation', the radio wave polarizations experience different permittivities, travel at different phase velocities, and produce a polarimetric phase shift. The polarimetric coherence method provides a way to measure the polarimetric phase shift from sounding data and hence infer horizontal anisotropy in the ice fabric. A full description of the method is given by Jordan and others (2019), with Dall (2010) providing the initial proof-of-concept.

The method works by cross-correlating orthogonal co-polarized radar signals, s_{hh} and $s_{\nu\nu}$, and measuring the relative phase shift as a function of ice depth. When applied to multipolarization plane data, the polarimetric coherence method pairs separate co-polarized measurements at 90 degrees, and considers the azimuthal behavior of the phase shift to infer the principal axes. Following Jordan and others (2019) we assume the convention that when $\theta=0^\circ$ the h polarization plane is aligned with the x-axis and the ν polarization plane is aligned with the y-axis (i.e. bins 1 and 5 in Fig. 2 are paired). $h-\nu$ polarization pairs are then generated as a function θ by pairing bins 2 and 6, 3 and 7, and 4 and 8 giving four independent pairs (Fig. 3).

For each h-v polarization pair the polarimetric coherence (also called *hhvv* coherence) is computed over a local depth window using the estimator

$$c_{hhvv}(\theta, z) = \frac{\sum_{j=1}^{N} s_{hh,j} \cdot s_{vv,j}^*}{\sqrt{\sum_{j=1}^{N} |s_{hh,j}|^2} \sqrt{\sum_{j=1}^{N} |s_{vv,j}|^2}},$$
 (3)

where N is the number of independent range bins, j is a summation index, * indicates complex conjugate, and the double subscripts indicate co-polarized measurements. c_{hhvv} is a complex number defined within the unit circle. The coherence magnitude, $|c_{hhvv}|$ is defined on [0,1] and quantifies the correlation between hh and vv measurements. The hhvv coherence phase

$$\phi_{hhvv}(\theta, z) = \arg(c_{hhvv}),$$
 (4)

provides a statistical estimate of the phase difference between hh and $\nu\nu$ measurements. The vertical phase gradient, $d\phi_{hh\nu\nu}/dz$, is used as a diagnostic for horizontal fabric properties and this is discussed in more detail in the Theoretical Background section.

From a mathematical analogy between Eqn (3) and the statistics of coherence estimation in radar interferometry (Touzi and Lopes, 1999), the Cramer–Rao bound can be used to estimate the error on ϕ_{hhvv} via

$$\sigma_{\phi_{hhvv}} pprox \frac{1}{|c_{hhvv}|} \sqrt{\frac{1 - |c_{hhvv}|^2}{2N}},$$
 (5)

where N is the number of independent range-bins (analogous to the equivalent number of looks in radar interferometry). Examples of $\sigma_{\phi_{hhv}}$ for different values of N are shown in Figure 4. In the data analysis we use depth windows of 40 and

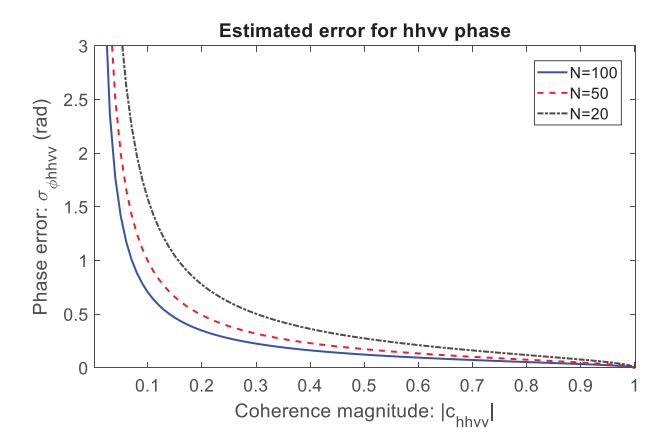


Fig. 4. *hhvv* phase error as a function of *hhvv* coherence magnitude and number of range bins, *N*.

20 m which, for the ApRES range resolution of \approx 0.43 m, corresponds to N = 93 and N = 47.

The application of Eqns (3) and (4) to an ice-sheet radar back-scatter model (Fujita and others, 2006; Jordan and others, 2019) implicitly assumes that we are considering the received signal phase rather than the de-ramped phase stored by the ApRES, Eqn (2). To assess the impact of de-ramping upon the coherence, we consider a term from the numerator of Eqn (3) which has proportionality

$$s_{hh}.s_{vv}^* \propto \exp\left(i\phi_{dhh}\right).\exp\left(-i\phi_{dvv}\right)$$
 (6)

for the de-ramped signal. Using Eqn (2) it follows that

$$s_{hh}.s_{vv}^* \propto \exp\left(-i\phi_{rhh}\right).\exp\left(i\phi_{rvv}\right)$$
 (7)

and hence the de-ramped signal has the opposite hhvv phase polarity to the received signal. To correct for this we replace c_{hhvv} with c_{hhvv} * but from herein do not notate this explicitly.

2.3.2. Polarimetric power

The polarimetric phase shift also results in modulation of radar power as a function of azimuthal angle, and past analyses have used this as an indicator of ice fabric anisotropy (Fujita and others, 2006; Matsuoka and others, 2012; Li and others, 2018). Following Matsuoka and others (2012) the co-polarized power anomaly can be calculated from the multi-polarization data via

$$\delta[P_i] = [P_i] - [\langle P \rangle], \tag{8}$$

where $[P_i]$ is the returned power of the ith bin, $[\langle P \rangle]$ is the mean power (averaged over all polarization planes) and the square bracket dB notation $[\chi] = 10\log_{10}(\chi)$ is assumed. Equation (8) assumes that all other aspects of the radar power equation (geometric spreading, attenuation loss, volume scattering) are independent of polarization and is typically calculated using a moving average or smoothing function with respect to the depth coordinate.

3. Theoretical Background

To interpret the polarimetric data analysis, we now summarize a formulation that relates ice fabric anisotropy to dielectric anisotropy (Fujita and others, 2006), including an original formulation of dielectric anisotropy in the near-surface (firn) layer. We then outline a commonly used polarimetric matrix backscatter model (Fujita and others, 2006), including its adaptation to model the

hhvv coherence phase (Jordan and others, 2019), and provide an overview of how the model is used to estimate horizontal fabric properties.

3.1. Dielectric model of ice fabric anisotropy

In this study the c-axis orientation distribution of the ice fabric is formulated in terms of a second-order orientation tensor (Woodcock, 1977; Montagnat and others, 2014). The tensor eigenvalues describe the relative concentration of c-axes aligned with each principal coordinate direction/eigenvector and have properties: $E_1 + E_2 + E_3 = 1$ and $E_3 > E_2 > E_1$ (Fujita and others, 2006). As in previous radar studies (Fujita and others, 2006; Drews and others, 2012; Brisbourne and others, 2019; Jordan and others, 2019) we assume that the E_3 eigenvector (the eigenvector corresponding to the E_3 eigenvalue) is vertical, with the E_1 and E_2 eigenvectors in the horizontal plane to be solved for from the data analysis. The E_2 eigenvector represents the direction of greatest horizontal c-axis alignment.

The appendix of Fujita and others (2006) describes an effective medium model that relates the orientation tensor to the bulk dielectric tensor. This approach is justified as the crystals are \sim mm in size and the radio wavelength is \sim m. This model results in a bulk (macroscopic) birefringence

$$\Delta \epsilon = \Delta \epsilon' (E_2 - E_1), \tag{9}$$

where $\Delta \epsilon' = (\epsilon_{\parallel c} - \epsilon_{\perp c})$ is the birefringence of an ice crystal with $\epsilon_{\parallel c}$ and $\epsilon_{\perp c}$ the dielectric permittivities for polarization planes parallel and perpendicular to the *c*-axis. The horizontal eigenvalue difference, $E_2 - E_1$, quantifies the horizontal asymmetry of the ice fabric. At ice-penetrating radar frequencies, $\Delta \epsilon' \approx 0.034$ (Fujita and others, 2000). Anisotropy in the conductivity of the crystal can be neglected as the bulk conductivity of polar ice is dominated by acidity content (Fujita and others, 2006).

In this study we interpret ice fabric/dielectric anisotropy in the near-surface (firn) which is described by a dielectric mixing model of (anisotropic) ice and (isotropic) air inclusions. In the Appendix we provide a derivation that generalizes the bulk birefringence for solid ice (Eqn (9)) to take into account the ice volume fraction, ν (the single additional variable compared to the solid-ice case). To first order, in terms of a small parameter expansion, this gives a result of the form

$$\Delta \epsilon_{\text{firn}} \approx f(\nu) \Delta \epsilon'(E_2 - E_1),$$
 (10)

where $0 \le v \le 1$ and f(v) is a polynomial function of v. f(v) is defined on [0,1] and can be interpreted as reduction factor for the birefringence of firn with respect to solid ice (Fig. 5). Due to the unavailability of firn density measurements in our study region (to best of our knowledge the closest example is $\sim 250 \text{ km}$ upstream (Alley and Bentley, 1988)) we do not use Eqn (10) explicitly, and instead use the solid-ice version, Eqn (9). However, the Appendix is included for the benefit of future studies where firn density measurements may be available.

3.2. Polarimetric backscatter model of an ice sheet

The polarimetric backscatter model is described in detail by Fujita and others (2006) and considers a nadir sounding geometry where the ice sheet is modeled as a stratified anisotropic medium and radar reflections are assumed to be specular. For the general case, the model incorporates the combined polarimetric effect of birefringent propagation (associated with smoothly varying fabric asymmetry) and anisotropic scattering (associated with local

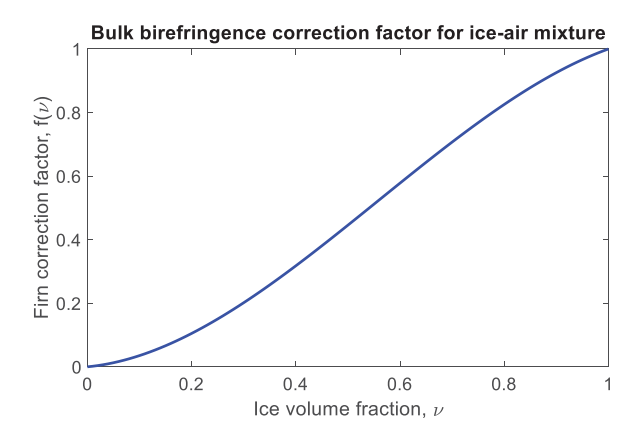


Fig. 5. Reduction factor for the birefringence of firn with respect to solid ice as a function of ice volume fraction, ν .

fabric discontinuities). Mathematically the model is formulated as a matrix product and has a functional dependence upon: α (the angle from the E_1 eigenvector to the h polarization, or equivalently, E_2 eigenvector to the ν polarization), δ (the polarimetric phase shift along the principal axes) and r (the anisotropic scattering coefficient ratio). The model is defined using Cartesian coordinates with the z-axis vertical and aligned with the E_3 eigenvector.

The backscatter model applies to the full ice column which, in general, contains different layers with varying layer orientation. In this study we are interested in using the model to perform fabric estimates for depth-sections where: (i) there is a suitably high coherence magnitude, (ii) the inferred ice fabric is consistent with a model of unchanging azimuthal orientation within a depth-section.

3.2.1. Using the model to estimate fabric orientation

The prevailing horizontal c-axis (E_2 eigenvector) is estimated by comparing observed azimuthal properties of the vertical phase gradient, $d\phi_{hh\nu\nu}/dz$ (measured with respect to θ) with modeled (simulated with respect to α). An advantage to using $d\phi_{hh\nu\nu}/dz$ (instead of $\phi_{hh\nu\nu}$) to infer fabric orientation is that it is not significantly impacted by propagation in anisotropic ice above the layer where fabric is being assessed.

Collating past results from Fujita and others (2006), Matsuoka and others (2012), Jordan and others (2019), we simulated the azimuth-phase dependence of $\delta[P]$ (Fig. 6a) and ϕ_{hhvv} (Fig. 6b) and $d\phi_{hhvv}/dz$ (Fig. 6c) for fixed bulk birefringence with depth-invariant principal axes and isotropic scattering (r=1).

When the incident polarization planes are aligned with the principal axes ($\alpha = 0^{\circ}$, 90°) they continue to propagate in a single polarization state throughout the medium and ϕ_{hhvv} is equivalent to δ and

$$\frac{\mathrm{d}\phi_{hhvv}(\alpha=0^{\circ}, 90^{\circ})}{\mathrm{d}z} = \pm \frac{\mathrm{d}\delta}{\mathrm{d}z} = \pm \frac{4\pi f_c}{c} \frac{\Delta\epsilon'(E_2 - E_1)}{2\sqrt{\epsilon_{ice}}}, \quad (11)$$

(Jordan and others, 2019). There is a positive *hhvv* phase gradient when $\alpha = 0^{\circ}$ as the ν polarization travels at a slower phase velocity than the h polarization (and *vice versa* when $\alpha = 90^{\circ}$). In practice, the orientation of the E_2 and E_1 eigenvectors are most easily inferred by matching the angular transitions between positive and negative phase gradient at $\alpha = 45^{\circ}$, $\alpha = 135^{\circ}$ to the data.

The differing azimuthal symmetry properties for $\phi_{hh\nu\nu}$ and $\delta[P]$ demonstrate an advantage to using the coherence method to infer fabric orientation. Specifically, $d\phi_{hh\nu\nu}$ has 180 degree azimuthal symmetry which matches the 180 degree azimuthal

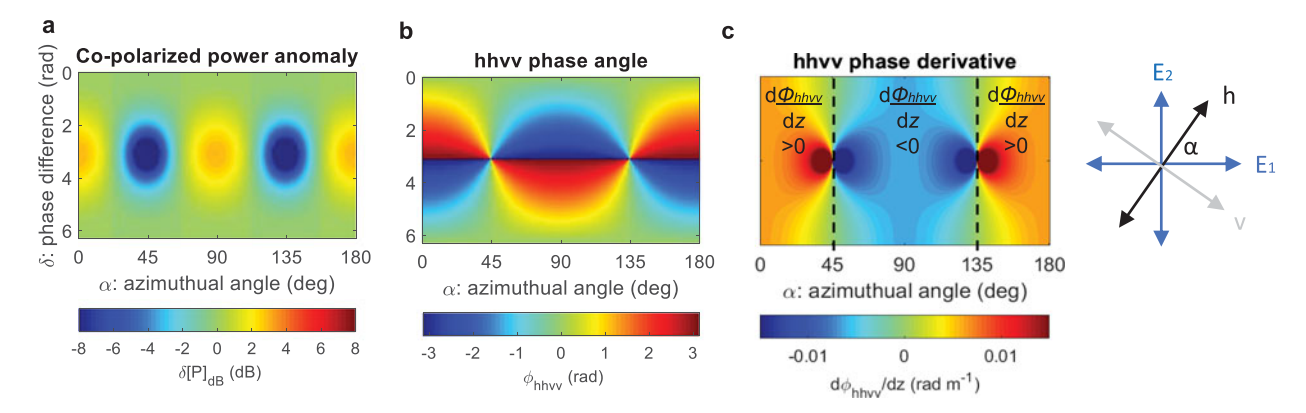


Fig. 6. Simulated dependence of polarimetric power and *hhvv* coherence phase for radio propagation in a birefringent ice sheet: (a) $\delta(P]$, (b) ϕ_{hhvv} , (c) $d\phi_{hhvv}/dz$. The definition of the principal angle, α , is shown in relation to the E_2 and E_1 eigenvectors and the h-v measurement system. Panel (a) considers a single set of co-polarized measurements (equivalent to hh) whereas panels (b) and (c) pair hh and vv measurements at 90 degree intervals. The angular dependence of $d\phi_{hhvv}/dz$ is used as a diagnostic for fabric orientation, and the '90 degree zones' of positive and negative gradients are marked in panel (c). Following Jordan and others (2019) the units in (c) assume a fixed bulk birefringence, $\Delta \epsilon = 0.0035$.

symmetry of the orientation tensor. On the other hand, $\delta[P]$ has 90 degree azimuthal symmetry. Due to this degeneracy (with respect to the 180 degree symmetry of the orientation tensor) there is therefore an angular ambiguity for the power if the measurement plane is perpendicular or parallel to the E_2 eigenvector.

Model simulations for $\phi_{hh\nu\nu}$ and $\delta[P]$ for anisotropic scattering $(r \neq 1)$ can be found in Jordan and others (2019), Fujita and others (2006) and Matsuoka and others (2012) respectively. For $\phi_{hh\nu\nu}$ the central result is that 180 degree azimuthal symmetry is preserved between isotropic and anisotropic scattering, enabling fabric orientation to be determined for different scattering regimes.

3.2.2. Using the model to estimate fabric asymmetry

Equation (11) indicates that E_2-E_1 (the horizontal eigenvalue difference) is proportional to $|\mathrm{d}\phi_{hh\nu\nu}(\alpha=0^\circ, 90^\circ)/\mathrm{d}z|$. As f_c and c are constants and ϵ_{ice} can be approximated as a constant, $|\mathrm{d}\phi_{hh\nu\nu}(\alpha=0^\circ, 90^\circ)/\mathrm{d}z|$ can be used to estimate E_2-E_1 . In Jordan and others (2019), low-pass filtering of $\phi_{hh\nu\nu}$ was used to evaluate $|\mathrm{d}\phi_{hh\nu\nu}/\mathrm{d}z|$ and obtain estimates for E_2-E_1 . However, in this study (due to there being limited regions of high coherence magnitude) we evaluate $|\mathrm{d}\phi_{hh\nu\nu}/\mathrm{d}z|$ using a linear approximation across a local depth window.

4. Results

4.1. Polarimetric coherence, power, and depth-range selection

Figure 7 shows the mean (polarization-averaged) power, co-polarized power anomaly, *hhvv* coherence magnitude and *hhvv* coherence phase from four example sites along the traverse. Data from the shallowest 500 m of ice was considered, as this marks the approximate depth where returned power was above the noise floor (\approx 80 dB) at all sites. Depth windows of 40 m were used in the coherence estimates corresponding to N=93 in Eqn (3). In the power plots there are eight independent measurements (due to the 22.5 degree angular resolution) with $\theta=0^\circ$ and $\theta=180^\circ$ identical. In the coherence plots there are four independent estimates ($\theta=0$, 22.5, 45 and 67.5°), with $\theta=90$, 112.5, 135, 157.5 and 180° generated by continuing the rotation pattern in Figure 3.

The ice fabric estimates were performed over depth intervals where the following three criteria were met. First, when there is relatively high $|c_{hh\nu\nu}|$ (an angular average of 0.3 or greater, which is informed by the $hh\nu\nu$ phase error relationship in Fig. 4). Second, the azimuthal properties of $d\phi_{hh\nu\nu}/dz$ conform

with the modeled azimuthal symmetry properties of $d\phi_{hhvv}/dz$ in Figure 6c (specifically, when there is evidence for '90 degree zones' of positive and negative phase gradient). This step tests if the principal axes can be considered unchanging in the depth interval. Third, the depth interval is sufficiently large to contain at least two separate coherence averaging windows, ensuring that the phase gradient estimates contain at least two independent sample regions.

At Site 2 (broadly representative of sites 1, 5 and 10) there is low $|c_{hh\nu\nu}|$ (generally < 0.25) at all depths. Therefore, at these sites ice fabric cannot be estimated at any ice depth. At Site 6 (broadly representative of sites 3, 4, and 9) there is high $|c_{hh\nu\nu}|$ (generally > 0.5) at all angles for depths < 50 m and ice fabric was estimated in the near-surface. At sites 7 and 8 there are bands of high $|c_{hh\nu\nu}|$ in both the near-surface and deeper ice ($\approx 170-280$ m and $\approx 280-360$ m respectively). At these sites we were able to estimate ice fabric in the near-surface and over these limited intervals in deeper ice.

Figure 7 confirms that low $|c_{hh\nu\nu}|$ is associated with a randomization of $\phi_{hh\nu\nu}$. By contrast, regions of high $|c_{hh\nu\nu}|$ are associated with greater phase continuity and there is evidence for vertical phase shifting in the regions highlighted by the pink bounding boxes in Figure 7. Previous work by Jordan and others (2019) demonstrated that a low-power SNR results in low $|c_{hh\nu\nu}|$. However, Figure 7 indicates that the converse is not necessarily true, and a high-power SNR does not guarantee high $|c_{hh\nu\nu}|$. For example, at ice depth $z\approx 100$ m the majority of the sites have low $|c_{hh\nu\nu}|$ whereas the power is ≈ 30 –40 dB above the noise floor. Suspected polarimetric decorrelation mechanisms include reflections from non-specular layers and reflections from non-parallel layers.

Figure 7 indicates that, at sites 7 and 8, the bands of high $|c_{hhvv}|$ in deeper ice are associated with 180° azimuthal power periodicity, likely due to a dominance of anisotropic scattering (Fujita and others, 2006; Matsuoka and others, 2012). However, at the angular resolution of the measurements (22.5°) it is difficult to separate 90° power periodicity (dominated by birefringent propagation) from 180° power periodicity. Figure 7 also indicates limited evidence for power anisotropy in the near-surface, but we will later show using the coherence method that fabric anisotropy is present.

4.2. Ice fabric estimates

Using the polarimetric coherence method the depth-azimuth properties of $d\phi_{hh\nu\nu}/dz$ were used to determine horizontal fabric

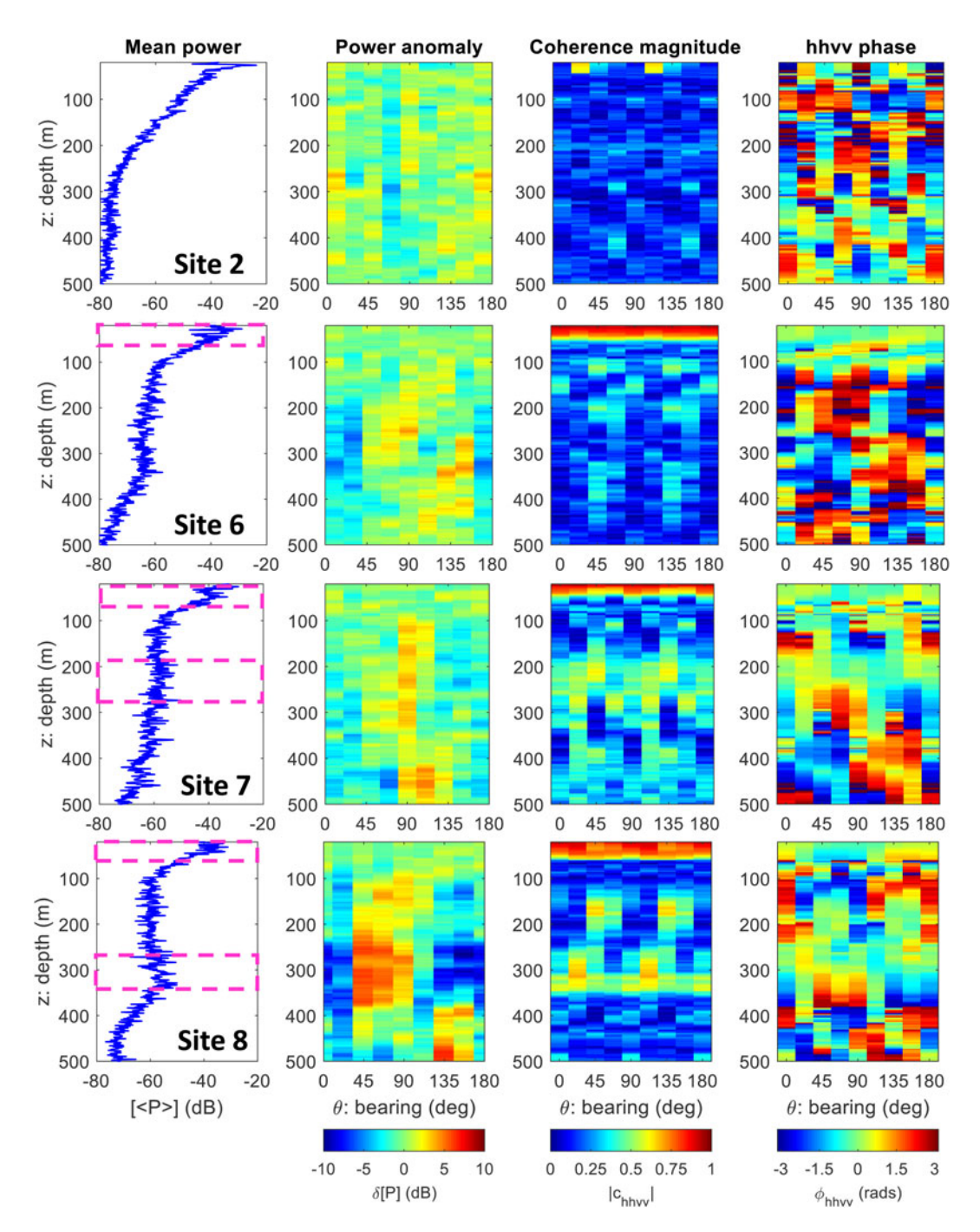


Fig. 7. Polarimetric power and coherence at four sites from the traverse. Far left: Mean (polarization-averaged) power. Center left: co-polarized power anomaly. Center right: *hhvv* coherence magnitude. Far right: *hhvv* phase angle. The approximate ice thicknesses are 805 m, 780 m, 760 m, 730 m at sites 2, 6, 7, 8. The pink dashed bounding boxes indicate depth intervals in the near-surface and deeper ice where $|c_{hhvv}|$ is sufficiently high for ice fabric estimates to be made. The angular coordinate, θ , is defined with respect to magnetic north/west (Fig. 2).

properties. Specifically, the measurement angle (θ) was referenced to the modeled angle (α) by identifying the angular transitions between positive–negative phase gradient $(\alpha=45^\circ)$ and negative–positive phase gradient $(\alpha=135^\circ)$ in Figure 6c, thereby enabling the principal axes $(\alpha=0,90^\circ)$ to be established. We then estimated horizontal ice fabric asymmetry (the E_2-E_1 eigenvalue difference) from $|\mathrm{d}\phi_{hhw}/\mathrm{d}z|$, Eqn (11).

Figure 8 shows c_{hhvv} and ϕ_{hhvv} at sites 7 and 8 over the depth intervals where the fabric estimates were made: the near-surface (defined here as z < 50 m), and deeper ice (170 < z < 280 m at Site 7 and 280 < z < 360 m at Site 8). In deeper ice, at both sites, the sign of $d\phi_{hhvv}/dz$ switches from positive to negative between $\theta = 22.5^{\circ}$ and $\theta = 45^{\circ}$, enabling $\alpha = 45^{\circ}$ to be

estimated as the average between these two values using $\theta \approx \frac{1}{2}(22.5+45)^{\circ} \approx 34^{\circ}$. Subsequently, comparing with the model simulation in Figure 6c, $\alpha=0^{\circ}$ was estimated to be $\theta \approx (34+135)^{\circ} \approx 169^{\circ}$ and $\alpha=90^{\circ}$ was estimated to be $\theta \approx (34+45)^{\circ} \approx 79^{\circ}$. To estimate fabric asymmetry in deeper ice, we then evaluated $|\mathrm{d}\phi_{hhvv}/\mathrm{d}z|$ for $\theta=0$, 67.5°, either side of the inferred principal angle of 79° using linear regression applied to Eqn (11). This is indicated by dashed lines in Figure 8 and gives $E_2-E_1\approx 0.19$ at Site 7 and $E_2-E_1\approx 0.21$ at Site 8.

The high coherence band in the near-surface persists to a depth $z \approx 50$ m. To ensure at least two independent depth regions were included in the fabric estimate the coherence averaging window was reduced to 20 m. Both near-surface plots in Figure 8

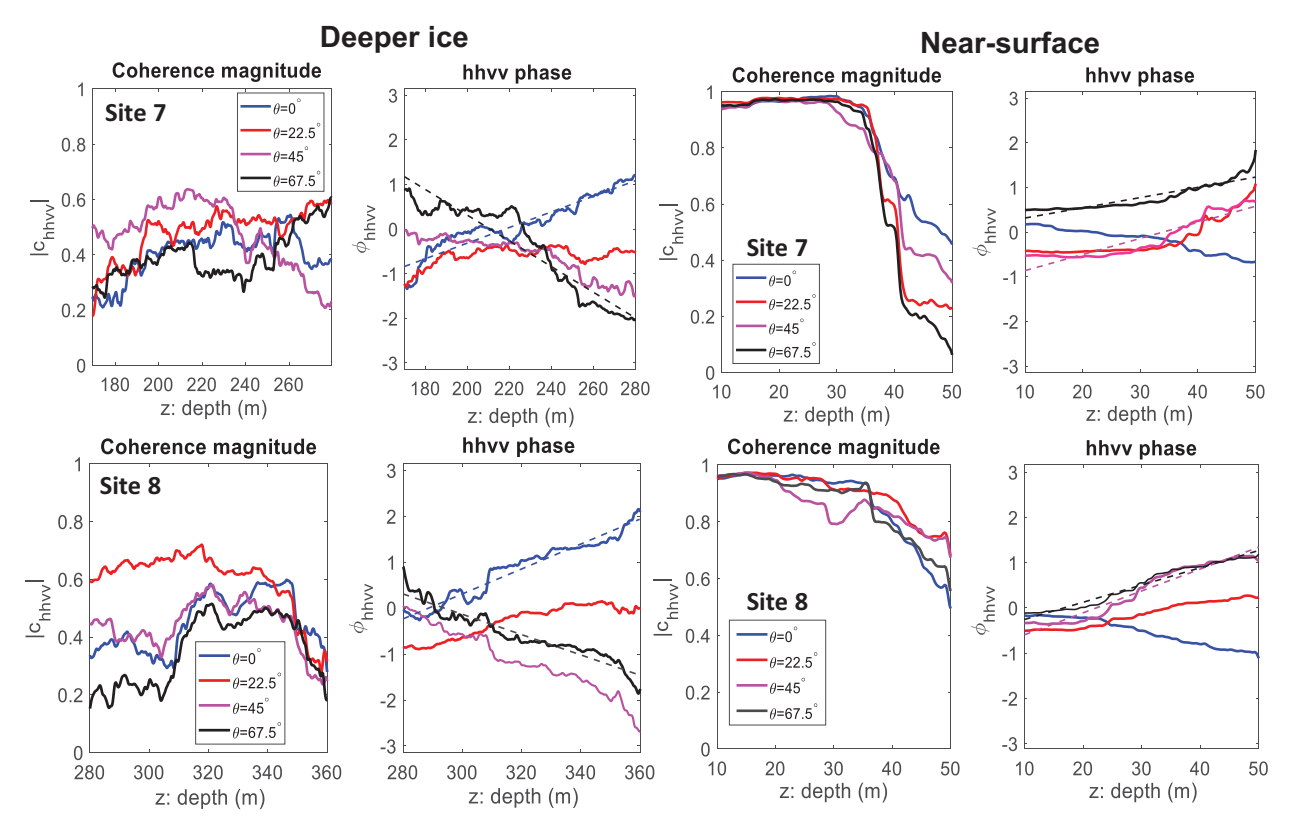


Fig. 8. Ice fabric estimates at sites 7 and 8 using the vertical phase gradient method. The regression lines (angles either side of the inferred principal axis) that are used to estimate the $E_2 - E_1$ eigenvalue difference are indicated.

indicate that the sign of $\mathrm{d}\phi_{hhvv}/\mathrm{d}z$ switches from negative to positive between $\theta=0^\circ$ and $\theta=22.5^\circ$ enabling $\alpha=135^\circ$ to be estimated using $\theta\approx\frac{1}{2}(0+22.5)^\circ\approx11^\circ$. Hence, comparing with the model simulation in Figure 6c, we can infer that $\alpha=0^\circ$ is estimated at $\theta\approx(11+45)^\circ\approx56^\circ$, and $\alpha=90^\circ$ is estimated at $\theta\approx(11+135)^\circ\approx146^\circ$ (45° and 135° correspond to the angular difference between the negative–positive transition in phase gradient and the principal axes). Following the same approach as deeper ice, we then evaluated $|\mathrm{d}\phi_{hhvv}/\mathrm{d}z|$ either side of the inferred principal angles, giving $E_2-E_1\approx0.23$ at Site 7 and $E_2-E_1\approx0.46$ at Site 8.

Due to only including two independent depth intervals in the coherence estimate (Eqn (3)) we did not propagate the $E_2 - E_1$ errors from the $|d\phi_{hhvv}/dz|$ regression slopes in Figure 8. (Each plot in Fig. 8 shows more than two points because a moving average is used in the coherence estimate.) Additionally, the following sources of bias could effect the estimation of $E_2 - E_1$. First, the angular uncertainty of the inferred principal angle is $\approx 20^{\circ}$ which, following the analysis in Appendix C by Jordan and others (2019), could result in estimation biases of up to $\pm \approx 20\%$ (positive and negative biases occur dependent upon the value of δ). Second, the transmit–receive antenna separation $(\approx 10 \text{ m})$ results in deviations from a vertically propagating wave in the near-surface (e.g. at 30 m depth this angular offset is estimated to be $\approx 5^{\circ}$). This scenario is mathematically equivalent to there being a tilt angle between the E_3 eigenvector and the vertical and a discussion of the estimation bias is provided in Appendix A by Jordan and others (2019). Third, from the relationship in Figure 5, it is predicted that a non-zero air volume fraction in the near-surface will lead to a minor underestimation in $E_2 - E_1$. Despite these limitations, all $E_2 - E_1$ estimates are physically plausible (in the allowed range $0 < E_2 - E_1$ < 0.5 given the constraint $E_3 > E_2 > E_1$) and yield consistent patterns.

4.3. Ice fabric estimates in relation to ice flow

Figure 9a summarizes ice fabric orientation estimates relative to the direction of ice flow. In the near-surface, the prevailing horizontal c-axis (E_2 eigenvector) is orientated consistently between sites, and is closer to perpendicular to flow. In deeper ice, the prevailing horizontal c-axis is also consistent between sites and aligned closer to parallel to flow. Also shown in Figure 9a are the principal strain-rate directions and relative magnitudes. The Cartesian strain rates were calculated from satellite-derived surface velocity measurements (Rignot and others, 2011, 2017), with a Gaussian-kernel, 2D-convolutional derivative with kernel standard deviation of 2 km. Gridded strain rates were then converted to principal strain rate magnitudes and directions through a coordinate transform of the strain rate tensor.

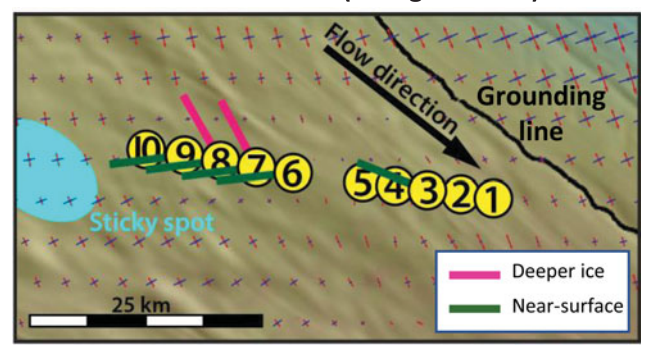
Figure 9b summarizes the magnitude of the fabric asymmetry (E_2 – E_1 eigenvalue difference) across the sites. In the near-surface, the magnitude of fabric asymmetry increases toward the center of Whillans Ice Stream (or, equivalently increases as the measurement sites get closer to the sticky spot). In deeper ice the magnitude of fabric asymmetry is similar at the two sites.

5. Discussion

5.1. Fabric development in ice sheets

To place our Whillans Ice Stream fabric results in context we now summarize fabric development in different stress regimes present in the ice sheets. The structure of a single ice crystal makes deformation along basal planes (perpendicular to the *c*-axis) over an order of magnitude more favorable, compared to deformation across basal planes (parallel to the *c*-axis) (Alley, 1988; Azuma, 1994). In polycrystalline ice, this result is also true in a statistical sense, where the orientations of individual *c*-axes modify the effective viscosity of the bulk material. The anisotropic

a Fabric orientation (E2 eigenvector)



b Fabric asymmetry and horizontal strain rate

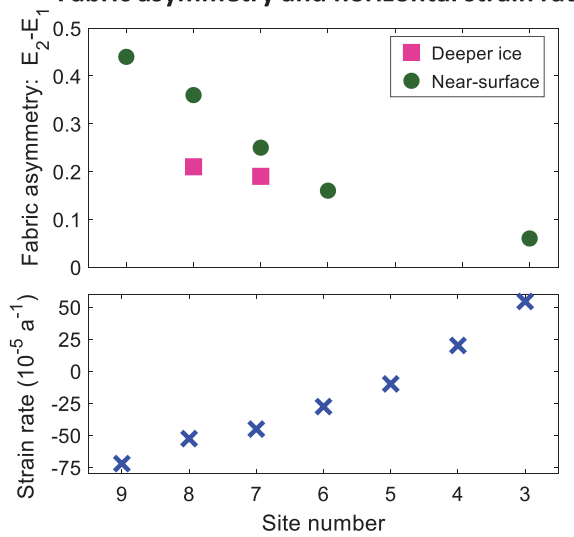


Fig. 9. (a) Summary of the orientation (prevailing horizontal c-axis/ E_2 eigenvector) of ice fabric estimates relative to ice motion. The pink and green lines illustrate the direction of the E_2 eigenvector (greatest horizontal c-axis concentration) in the deeper ice and the near-surface. The red and blue crossed arrows indicate the principal strain rate vectors (extension and compression) computed from the ice surface velocity (Rignot and others, 2011, 2017). (b) Magnitude of fabric asymmetry ($E_2 - E_1$ eigenvalue difference) across the survey transect (upper plot) compared with minimum principal horizontal strain rate (lower plot). Negative strain rates correspond to compression.

deformation behavior of individual ice crystals results in the *c*-axes continuously migrating toward the direction of maximum compression, and the fabric developing a preferential orientation.

Preferential fabric orientation has been observed in ice cores at ice domes where the vertical compression of ice causes the c-axes to preferentially align vertically (Gow and Williamson, 1976; Wang and others, 2002). In the limiting case this fabric is referred to a 'single maximum' ($E_3 \approx 1$, $E_2 \approx E_1 \approx 0$ in terms of the fabric eigenvalues). From Eqn (11) this vertical anisotropy appears as isotropic to radar sounding measurements. In regions where a lateral component of tension is present, such as ice divides or ice rises, the c-axes tend to align in a plane orthogonal to the flow/extension direction (Wang and others, 2002; Weikusat and others, 2017; Brisbourne and others, 2019). In the limiting case, this fabric is referred to as a 'vertical girdle' ($E_3 \approx E_2 \approx \frac{1}{2}$, $E_1 \approx 0$ in terms of the fabric eigenvalues). From Eqn (11) this horizontal anisotropy can be detected by radar sounding measurements.

In contrast with ice divides and domes there has been more heterogeneity observed in ice fabric that forms in ice streams (Jackson and Kamb, 1997; Horgan and others, 2011; Picotti and others, 2015; Smith and others, 2017), illustrating the diversity of stress regimes that can be present. Specifically, ice in fast flow can exhibit the following fabrics:

- 1. A single maximum. The Whillans Ice Stream trunk was inferred from multi-component seismic data to exhibit a single-maximum fabric in deeper ice, with the near-surface firn layer approximately a random fabric (Picotti and others, 2015). This is consistent with unconfined thinning of Whillans Ice Stream associated with downstream acceleration.
- 2. A vertical girdle where the prevailing horizontal c-axis is perpendicular to flow. This was inferred from shear wave splitting seismic data at Rutford Ice Stream by Smith and others (2017), and was more precisely referred to as a horizontal partial girdle. It occurs due to the combination of longitudinal extension and lateral confinement.
- 3. A vertical girdle where the prevailing horizontal c-axis is parallel to flow. This was inferred from active-source seismic data at Thwaites Glacier, West Antarctica by Horgan and others (2011). It occurs in regions where englacial deformation is dominated via the interaction with bed topography, in particular upstream features (Picotti and others, 2015).
- 4. A multiple-maximum fabric perpendicular to the shear plane. This was observed by Jackson and Kamb (1997) from direct samples (300 m deep boreholes) near to the shear margin of Whillans Ice Stream, and results from simple-shear glide with re-crystallization.

5.2. Interpretation of radar fabric measurements within Whillans ice stream

The fabric orientation result for the near-surface in Figure 9a corresponds to the second class of fabric described above (prevailing horizontal c-axis flow-perpendicular). This result is consistent with migration toward the compressive strain rate axis and the orientation of the surface strain components. This result suggests that the near-surface fabric is sensitive to the deformational regime of the surface ice. The fabric orientation result for deeper ice in Figure 9a corresponds to the third fabric type described above (prevailing horizontal c-axis flow-parallel). This result is consistent with englacial ice reacting to longitudinal compression associated with basal resistance from the nearby sticky spot. However, it is not consistent with the surface strain rates (as the compression axis is approximately perpendicular to the horizontal c-axis orientation).

In our radar study we established the presence of greater azimuthal fabric anisotropy (both within the ice column and regarding the development of near-surface anisotropy) than the seismic study of the region by Picotti and others (2015). However, Picotti and others (2015) predict that, away from their study region, the *c*-axes will rotate away from vertical and into the flow direction as longitudinal stresses become more compressive. Specifically, this is expected to occur in the downstream portion of Whillans Ice Stream, where it interacts with discrete sticky spots (Luthra and others, 2016), and the grounding line (Bindschadler and others, 1987), shown in Figure 1. This places the ice in our study area in a more complex deformation regime than purely longitudinal extension, potentially reconciling our result in deeper ice with Picotti and others (2015).

The inferred fabric strengths in deeper ice $(E_2-E_1\approx 0.2)$ correspond to a moderately strong vertical girdle fabric (limiting case $E_2-E_1=0.5$). This azimuthal anisotropy is broadly comparable to the maximum azimuthal anisotropy observed in the Greenland ice cores: NEEM (North Greenland Eemian Ice), GRIP (Greenland Ice Core Project) and NorthGRIP (Montagnat and others, 2014). The West Antarctic Ice Sheet divide (Kluskiewicz and others, 2017) and South Pole (Voigt, 2017) Antarctic ice cores both exhibit a stronger maximum azimuthal anisotropy, where E_2-E_1 is close to the limiting-case of a vertical girdle fabric.

5.3. Radar-derivation of ice fabric and recommendations for future surveys

This study underscores the fact that the polarimetric coherence method is better suited than radar power in estimating spatial variation ice fabric. Specifically, the analyses of radar power do not show clear evidence for near-surface fabric anisotropy and do not provide clear constraints on fabric strength and orientation. The polarimetric coherence magnitude, $|c_{hhvv}|$, provides a metric to assess where in the ice column fabric can be reliably estimated. We therefore recommend that $|c_{hhvv}|$ should be calculated in the field at the time of polarimetric data acquisition, enabling for a survey site location to be adjusted or for increased stacking to be applied during data acquisition.

As implemented by previous studies (Fujita and others, 2006; Matsuoka and others, 2012) we recommend taking multipolarization measurements at a slightly higher angular resolution (e.g. 15 degrees) than the 22.5 degrees used in this study. This higher angular resolution will enable more accurate estimates of the fabric orientation and asymmetry (Jordan and others, 2019). Alternatively, a single set of quad-polarized (fully polarimetric) measurements could be used to reconstruct co-polarized data at a given azimuthal angle and then estimate the fabric as described in this study. This approach would have the advantage of improving the angular accuracy of the fabric orientation estimate but is dependent upon the SNR of the cross-mode terms, s_{hv} , s_{vh} .

Finally, the estimation of horizontal fabric properties using the coherence method compliments seismic methods for characterizing ice fabric, better suited for recovering vertical fabric properties (Picotti and others, 2015; Brisbourne and others, 2019). The directional sensitivity of these two classes of geophysical method will potentially enable a complete 3D characterization of ice fabric.

6. Summary and Conclusions

This study adapted a polarimetric coherence method (Dall, 2010; Jordan and others, 2019) to estimate ice fabric using the ApRES. The method was trialed in a fast-flow region of West Antarctic, near to the suture zone of Whillans and Mercer ice streams where a basal sticky spot is present. The method enabled estimation of the prevailing horizontal c-axis (E_2 eigenvector) and magnitude of the horizontal fabric asymmetry ($E_2 - E_1$ eigenvalue difference). Furthermore, it provided a means to infer spatial patterns in the fabric (both within the ice column and between measurement sites).

In Whillans Ice Stream, the method demonstrated repeatable results in both the near-surface ($z < 50 \,\mathrm{m}$) and deeper ice ($z \approx 170 - 360 \,\mathrm{m}$), revealing a rotation in the prevailing horizontal c-axis with ice depth and rapid local development of fabric asymmetry in the near-surface. In the near-surface the inferred fabric properties are consistent with the surface compression direction, whereas in deeper ice the inferred fabric properties are consistent with englacial ice reacting to longitudinal compression associated with basal resistance from the nearby sticky spot.

Acknowledgments. TMJ would like to acknowledge support from EU Horizons 2020 grant 747336-BRISRES-H2020-MSCA-IF-2016. DMS would like to acknowledge partial support from an NSF CAREER award. Field data collection was supported by NSF grant ANT-1543441 as part of the SALSA project. We thank Julian Hanna, Sarah Neuhaus, Marino Protti and Aurora Roth for data collection assistant and UNAVCO, Antarctic Support Contract, Kenn Borek Air and the New York Air National Guard for logistic support. We would like to thank Jørgen Dall, Technical University of Denmark, and Carlos Martin and Alex Brisbourne, British Antarctic Survey, for their helpful comments.

References

Alley RB (1988) Fabrics in polar ice sheets: development and prediction. *Science* **240**(4851), 493–495.

- Alley RB and Bentley CR (1988) Ice-core analysis on the siple coast of West Antarctica. *Annals of Glaciology* 11, 1–7.
- Azuma N (1994) A flow law for anisotropic ice and its application to ice sheets. Earth and Planetary Science Letters 128, 601–614. doi: 10.1016/0012-821X(94)90173-2.
- Bindschadler RA, Stephenson SN, MacAyeal DR and Shabtaie S (1987) Ice dynamics at the mouth of ice stream B, Antarctica. *Journal of Geophysical Research: Solid Earth* **92**(B9), 8885–8894.
- Brennan PV, Lok LB, Nicholls K and Corr H (2014) Phase-sensitive FMCW radar system for high-precision Antarctic ice shelf profile monitoring. *IET Radar Sonar Navigation* 8(February 2013), 776–786. doi: 10.1049/iet-rsn. 2013.0053.
- Brisbourne AM and 5 others (2019) Constraining recent ice flow history at Korff ice rise, West Antarctica, using radar and seismic measurements of ice fabric. *Journal of Geophysical Research: Earth Surface* 124, 175–194– 373. doi: 10.1029/2018IF004776.
- Dall J and 8 others (2009) ESA's polarimetric airborne radar ice sounder (POLARIS): design and first results. IET Radar, Sonar and Navigation 4 (3), 488–496. doi: 10.1049/iet-rsn.2009.0035.
- Dall J (2010) Ice sheet anisotropy measured with polarimetric ice sounding radar. In 30th International Geoscience and Remote Sensing Symposium (IGARSS 2010), 25–30 July 2010, Honolulu, HI, USA, 2507–2510.
- Diez A and Eisen O (2015) Seismic wave propagation in anisotropic ice part 1: elasticity tensor and derived quantities from ice-core properties. *The Cryosphere* **9**(1), 367–384. doi: 10.5194/tc-9-367-2015.
- Drews R and 5 others (2012) Potential mechanisms for anisotropy in ice-penetrating radar data. *Journal of Glaciology* 58(209), 613–624. doi: 10. 3189/2012JoG11J114.
- Fujita S, Maeno H and Matsuoka K (2006) Radio-wave depolarization and scattering within ice sheets: a matrix-based model to link radar and ice-core measurements and its application. *Journal of Glaciology* 52(178), 407–424.
- Fujita S, Matsuoka T, Ishida T, Matsuoka K and Mae S (2000) A summary of the complex dielectric permittivity of ice in the megahertz range and its applications for radar sounding of polar ice sheets. *Physics of Ice Core Records* 104, 185–212.
- Gow AJ and Williamson T (1976) Rheological implications of the internal structure and crystal fabrics of the West Antarctic ice sheet as revealed by deep core drilling at Byrd Station. Geological Society of America Bulletin 87(12), 1665–1677.
- Haran T, Bohlander J, Scambos T and Fahnestock M (2005) MODIS mosaic of Antarctica (MOA) image map. National Snow and Ice Data Center, Boulder, CO. Digital media. http://nsidc.org/data/nsidc-0280.html.
- Hargreaves ND (1977) The polarization of radio signals in the radio echo sounding of ice sheets. *Journal of Physics D: Applied Physics* 10, 1285–1304.
 Hay MJ (2017) *Stability and Uncertainty of Ice-Sheet Crystal Fabrics* (Ph.D. thesis). University of Washington.
- Horgan HJ, Anandakrishnan S, Alley RB, Burkett PG and Peters LE (2011)
 Englacial seismic reflectivity: imaging crystal-orientation fabric in West Antarctica. *Journal of Glaciology* 57(204), 639–650.
- Jackson M and Kamb B (1997) The marginal shear stress of ice stream B, West Antarctica. Journal of Glaciology 43(145), 415–426. doi: 10.3189/ S0022143000035000.
- Jordan TM, Schroeder DM, Castelletti D, Li J and Dall J (2019) A polarimetric coherence method to determine ice crystal orientation fabric from radar sounding: application to the NEEM ice core region. IEEE Transactions on Geoscience and Remote Sensing. doi: 10.1109/TGRS. 2019.2921980.
- Kendrick AK and 12 others (2018) Surface meltwater impounded by seasonal englacial storage in West Greenland. Geophysical Research Letters 45, 1–8. doi: 10.1029/2018GL079787.
- Kingslake J, Martin C, Arthern RJ, Corr HFJ and King EC (2016) Ice-flow reorganization in West Antarctica 2.5 kyr ago dated using radar-derived englacial flow velocities. *Geophsyical Research Letters* 42, 9103–9112. doi: 10.1002/2016GL070278.
- Kluskiewicz D and 5 others (2017) Sonic methods for measuring crystal orientation fabric in ice, and results from the West Antarctic Ice Sheet (WAIS) Divide. *Journal of Glaciology* 63(240), 603–617. doi: 10.1017/jog. 2017.20.
- Li J and 8 others (2018) Multi-channel and multi-polarization radar measurements around the NEEM site. The Cryosphere 12, 2689–2705.
- Looyenga H (1965) Dielectric constants of heterogeneous mixtures. *Physica* 31, 401–406.

Luthra T, Anandakrishnan S, Winberry JP, Alley RB and Holschuh N (2016) Basal characteristics of the main sticky spot on the ice plain of Whillans Ice Stream, Antarctica. *Earth and Planetary Science Letters* **440**, 12–19

Matsuoka K, Power D, Fujita S and Raymond CF (2012) Rapid development of anisotropic ice-crystal-alignment fabrics inferred from englacial radar polarimetry, central West Antarctica. *Journal of Geophysical Research: Earth Surface* 117(3), 1–16. doi: 10.1029/2012JF002440.

Minchew BM, Meyer CR, Robel AA, Gudmundsson GH and Simons M (2018) Processes controlling the downstream evolution of ice rheology in glacier shear margins: case study on Rutford ice stream, West Antarctica. *Journal of Glaciology* **64**(248), 583–594. doi: 10.1017/jog.2018.47.

Montagnat M and 5 others (2014) Fabric along the NEEM ice core, Greenland, and its comparison with GRIP and NGRIP ice cores. The Cryosphere 8, 1129–1138. doi: 10.5194/tc-8-1129-2014.

Nicholls KW and 5 others (2015) Instruments and methods a ground-based radar for measuring vertical strain rates and time-varying basal melt rates in ice sheets and shelves. *Journal of Glaciology* **61**(230), 1079–1087. doi: 10. 3189/2015JoG15J073.

Picotti S, Vuan A, Carcione JM, Horgan HJ and Anandakrishnan S (2015) Anisotropy and crystalline fabric of Whillans Ice Stream (West Antarctica) inferred from multicomponent seismic data. *Journal of Geophysical Research: Solid Earth* 120, 4237–4262, doi: 10.1002/2014JB011591.

Rignot E, Mouginot J and Scheuchl B (2011) Ice flow of the Antarctic ice sheet. *Science* 33(6048), 1427–1430. doi: 10.1126/science.1208336.

Rignot E, Mouginot J and Scheuchl B (2017) MEaSUREs InSARBased Antarctica ice velocity map. Version 2, Boulder, Colorado USA, NASA National Snow and Ice Data Center Distributed Active Archive Center. Available at https://doi.org/10.5067/D7GK8F5J8M8R.

Smith EC and 5 others (2017) Ice fabric in an Antarctic ice stream interpreted from seismic anisotropy. Geophysical Research Letters 44, 3710–3718. doi: 10.1002/2016GL072093.

Touzi R and Lopes A (1999) Coherence estimation for SAR imagery. *IEEE Transactions of Geoscience and Remote Sensing* **37**(1), 135–149.

Vazquez-Roy JL, Krozer V and Dall J (2012) Wideband dual-polarization microstrip patch antenna array for airborne ice sounder. IEEE Antennas and Propagation Magazine 54(4), 98–107. doi: 10.3189/ 17275640278181730.

Voigt DE (2017) c-axis fabric of the South pole ice core. SPC14. U.S. Antarctic Program (USAP) Data Center. Dataset. doi: 10.15784/601057.

Wang Y and 5 others (2002) A vertical girdle fabric in the NorthGRIP deep ice core. *Journal of Glaciology* 35, 515–520. doi: 10.3189/17275640278181730.

Weikusat I and 10 others (2017) Physical analysis of an Antarctic ice core: towards an integration of micro- and macrodynamics of polar ice. Philosophical Transactions of The Royal Society A 375(2086), 20150347. doi: 10.1098/rsta.2015.0347.

Woodcock N (1977) Specification of fabric shapes using an eigenvalue method. Geological Society of America Bulletin 88, 1231–1236.

Young TJ and 8 others (2018) Resolving the internal and basal geometry of ice masses using imaging phase-sensitive radar. *Journal of Glaciology* 64, 649–660. doi: 10.1017/jog.2018.54.

Appendix

The effective medium model of fabric anisotropy in the firn layer combines the fabric orientation tensor formulation in the appendix of Fujita and others (2006) with the Looyenga mixing relations (Looyenga, 1965) for the two component mixture between ice and air, parameterized by the ice–air volume fraction, ν . The derivation assumes that the air inclusions are isotropic with dimensions much less than the radar wavelength and that dielectric anisotropy arises purely due to the real component of the dielectric permittivity of ice crystal grains.

Following Fujita and others (2006), the principal permittivities of the ice component can be expressed in terms of the eigenvalues of the orientation tensor as

$$\epsilon_{ii} = \epsilon_{\perp c} + \Delta \epsilon' E_i,$$
 (A1)

with the index i = 1, 2, 3. For an ice–air mixture, the Looyenga mixing relations for the effective permittivity are of the form

$$\epsilon_{\text{eff}} = \left(\nu \epsilon_{\text{ice}}^{1/3} + (1 - \nu)\right)^3, \tag{A2}$$

where the permittivity of air is assumed to be unity. Substituting ϵ_{ii} for ϵ_{eff} in Eqn (A2) gives the following formula for the principal, effective, permittivities

$$\epsilon_{ii}^{\text{eff}} = \left(\nu(\epsilon_{\perp c} + \Delta \epsilon' E_i)^{1/3} + (1 - \nu)\right)^3. \tag{A3}$$

We now wish to derive a formula for the bulk birefringence of the ice–air mixture in the horizontal plane $\Delta\epsilon=\epsilon_{21}^{\rm eff}-\epsilon_{11}^{\rm eff}$. To do this in an analytically tractable way we can rewrite Eqn (A3) in the form

$$\epsilon_{ii}^{\text{eff}} = \left(\nu \epsilon_{i}^{1/3} (1 + X_i)^{1/3} + (1 - \nu)\right)^3,$$
 (A4)

where $X_i = \Delta \epsilon' E_i / \epsilon_{1c}$ is a small parameter ($\approx \frac{1}{100}$ or less). Following a first-order Taylor expansion of $(1 + X_i)^{1/3}$, and then expanding the cubic to first order in X_i , we arrive at

$$\epsilon_{ii}^{\text{eff}} \approx \nu^{3} \epsilon_{\perp c} (1 + X_{i}) + \nu^{2} (1 - \nu) \epsilon_{\perp c}^{2/3} (1 + 2X_{i}/3)
+ \nu (1 - \nu)^{2} \epsilon_{\perp c}^{1/3} (1 + X_{i}/3) + (1 - \nu)^{3}.$$
(A5)

Subsequently, upon cancelation of zeroth-order terms when subtracting, the birefringence of the ice-air mixture is given by

$$\Delta \epsilon_{\text{firn}} = \epsilon_{22}^{\text{eff}} - \epsilon_{11}^{\text{eff}} \approx f(\nu) \Delta \epsilon'(E_2 - E_1), \tag{A6}$$

where

$$f(\nu) = \frac{1}{\epsilon_{\perp c}} \left(\nu^3 \epsilon_{\perp c} + \frac{2}{3} \nu^2 (1 - \nu) \epsilon_{\perp c}^{2/3} + \frac{1}{3} \nu (1 - \nu)^2 \epsilon_{\perp c}^{1/3} \right), \tag{A7}$$

is a third-order polynomial in v.